Volume 18 | Number 5 | May 2019 | Pages 931–1292

Photochemical & Photobiological Sciences

An international journal

rsc.li/pps

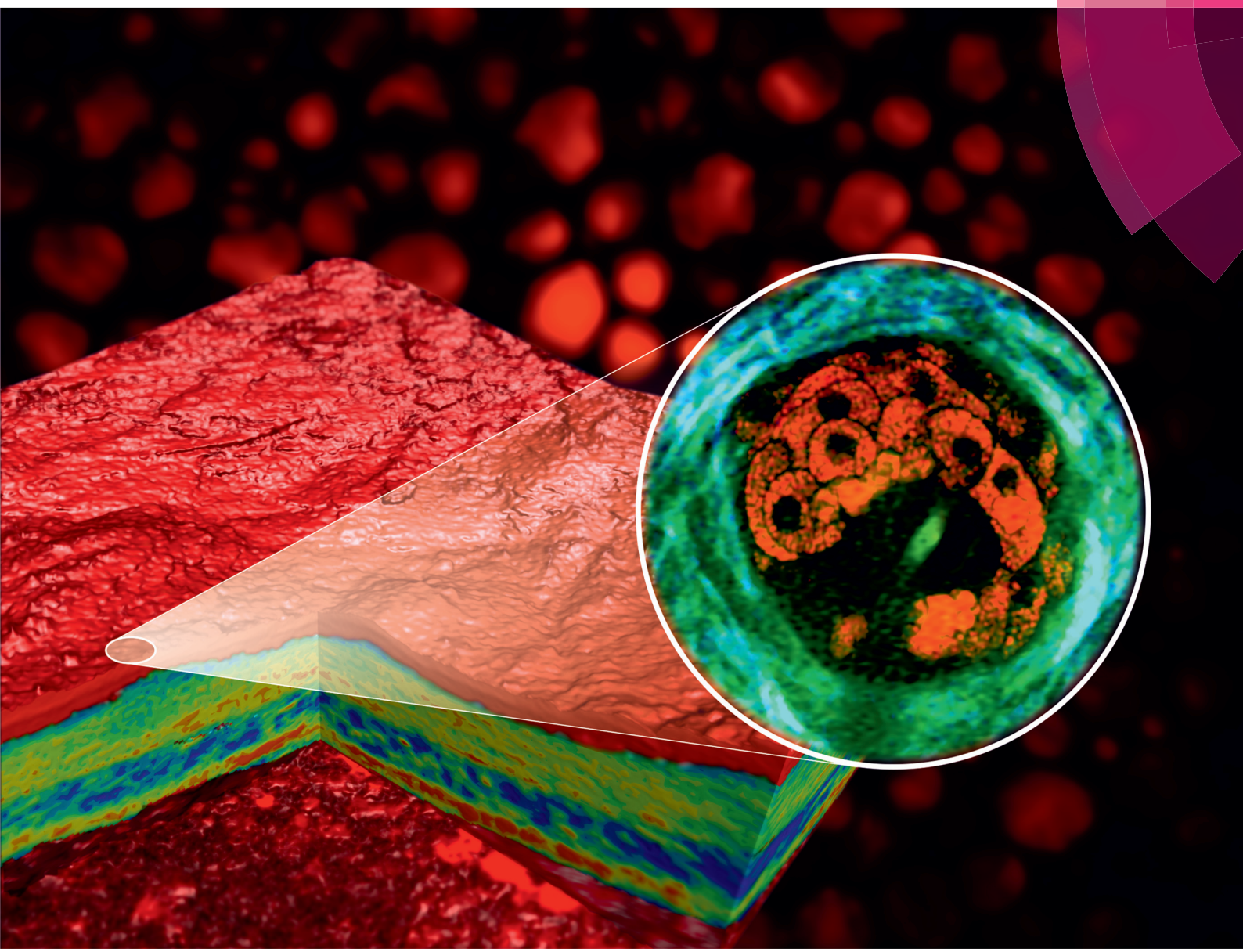

ISSN 1474-905X

ROYAL SOCIETY OF CHEMISTRY | Celebrating IYPT 2019

EPA ESP KOREAN SOCIETY OF PHOTOSCIENCE AOSP

Photochemical & Photobiological Sciences

PAPER

View Article Online
View Journal | View Issue

Cite this: *Photochem. Photobiol. Sci.*, 2019, **18**, 997

Depth resolved label-free multimodal optical imaging platform to study morpho-molecular composition of tissue

Marco Andreana, Ryan Sentosa, Mikael T. Erkkilä, Wolfgang Drexler and Angelika Unterhuber *

Received 18th September 2018,
Accepted 8th January 2019

DOI: 10.1039/c8pp00410b

rsc.li/pps

Multimodal imaging platforms offer a vast array of tissue information in a single image acquisition by combining complementary imaging techniques. By merging different systems, better tissue characterization can be achieved than is possible by the constituent imaging modalities alone. The combination of optical coherence tomography (OCT) with non-linear optical imaging (NLOI) techniques such as two-photon excited fluorescence (TPEF), second harmonic generation (SHG) and coherent anti-Stokes Raman scattering (CARS) provides access to detailed information of tissue structure and molecular composition in a fast, label-free and non-invasive manner. We introduce a multimodal label-free approach for morpho-molecular imaging and spectroscopy and validate the system in mouse skin demonstrating the potential of the system for colocalized acquisition of OCT and NLOI signals.

Introduction

Biomedical optical spectroscopy and imaging has been established as a powerful technique to study structure, function and biochemical composition of tissues. Measurements can be performed on molecules, organelles, proteins, cells, and in recent years even entire organisms.[1] In particular, multimodal non-linear optical imaging (NLOI) has the potential to inspect, analyse and track the molecular distribution in a label-free and non-invasive manner in real-time relying on different contrast mechanisms.[2–4] These techniques combine submicron isotropic spatial resolution with intrinsic three dimensional sectioning, and provide minimal photo-damage as well as reduced photo-toxicity due to the use of near infrared (NIR) light.[5] Such a combination gives a clear insight into the complex organization of biological structures.[6] Ultra-short high intensity light waves interact with the sample in such a way that a change in radiation is induced which can be captured by a photodetector. All these techniques can be conveniently carried out with laser-scanning microscopes (LSM) featuring rapid imaging capabilities and they are all easy to use for routine imaging applications. A typical laser-scanning NLOI microscope incorporates several detectors for detection of various non-linear optical signals simultaneously, enabling multimodal imaging for screening,[7] diagnosis and interventional guidance purposes,[8,9] as well as efficient monitoring of disease progression and treatment response by analysis of different image contrasts.[10]

Two-photon excited fluorescence (TPEF) is currently the most common and popular variant of NLOI, visualizing exogenous or endogenous fluorophores related to electronic transition from the excited to the ground state of a molecule involving two-photon excitation of the sample. This gives molecule-specific fluorescent emission of a photon from a lower energy emissive state, with both quantum yield and lifetime as intrinsic molecular parameters.[5,11] Biological tissues contain many sub-cellular components that are fluorescent and based on the wealth of these endogenous fluorophores, label-free tissue autofluorescence can be used as a parameter to evaluate biochemical and metabolic changes. This method has various applications in the medical field, such as the analysis of metabolic deterioration under ischemic necrosis[12] and depth dependent metabolism in skin keratinocytes.[13] These fluorescent components can either be intracellular or extracellular, and they are either composed of vitamins (or vitamin derivatives) such as retinol, cholecalciferol, riboflavin or pyridoxine, or aromatic amino acids including tyrosine, phenylalanine and tryptophan. Vitamin-based fluorophores tend to emit in the visible light range, while those containing aromatic amino acids emit in the UV range.[14–18] Intracellular endogenous fluorophores are connected to the cell or tissue type. Nicotinamide adenine dinucleotide (NADH) and its phosphate derivative (NADPH), and flavins as flavin adenine dinucleotide

Medical University of Vienna, Center for Medical Physics and Biomedical Engineering, Waehringer Guertel 18-20, 1090 Vienna, Austria.
E-mail: angelika.unterhuber@meduniwien.ac.at; Fax: +43-1-40400-39880; Tel: +43-1-40400-39223

(FAD) are important biomarkers associated with cellular metabolism, but also retinol, tryptophan, serotonin, melatonin, melanin, porphyrins and lipofuscin are relevant for different tissue types. Extracellular endogenous fluorophores on the other hand, comprise collagen and elastin. The extracellular matrix (ECM) in particular, which is composed of collagen networks, is involved in many pathologies, *e.g.* in tumour microenvironment remodelling.[19]

Fluorescence offers unprecedented sensitivity due to the intense electronic transition dipole moment. However, many samples are intrinsically non-fluorescent or only weakly fluorescent and saturation might pose a problem since the excited electrons remain in the excited state for a few nanoseconds before returning to the ground state to become available for another excitation. In addition, exogenous fluorescent labels are perturbative and not recommended for *in vivo* medical applications. Hence, additional optical imaging methods with high sensitivity and specific complementary molecular contrasts are highly desirable.

Second harmonic generation (SHG) is another two-photon process where simultaneous two-photon interaction produces an optical signal with twice the energy (or half the wavelength) of the incident photons. Since no molecules are excited to electronic or vibrational states, photo-toxicity and photo-bleaching are prevented. This non-resonant process is ultra-fast because the lifetime of the virtual state is in the order of only a few femtoseconds. Hence, electrons are always available for further excitation without saturation, even over increasing excitation intensity. Furthermore, unlike TPEF, SHG is energy conserving, meaning there is no non-radiative energy loss during the relaxation of the excited state. In particular SHG, being sensitive to molecular symmetry breaking, has found widespread applications in imaging certain biological materials as collagen type I fibers, microtubules (tubulin), and the highly polarizable myosin found in muscles, as these materials are assembled from fairly ordered, large non-centrosymmetric structures.[20,21] The potential of this technique has been shown in imaging both collagen distribution[15,20] and membrane potential.[22] Alteration of biological materials affects the level of SHG obtained from the imaged tissue, making it a useful optical property for diagnostic purposes in pathologic tissue[14] where a change in the collagen arrangement can be observed.[19,23]

TPEF and SHG can easily be combined in multimodal settings.[5,15,24,25] Various studies have utilized the combination on unstained tissue sections to observe the morphological changes that arise in diseased or cancerous tissues and to generate images, with information content comparable to standard haematoxylin-eosin (HE) stained slides typically used by pathologists.[14,26,27] Although studies have shown the potential of this combination as a substitute to conventional histopathological diagnosis, there are still associated limitations.

The wide range of biological materials not exhibiting strong optical transitions to electronic states in the visible and NIR wavelength regions can be investigated with coherent Raman scattering (CRS) microscopy to obtain vibrational spectroscopic contrast. CRS is one of the fast NLOI modalities with vibrational contrast and drives a vibrational transition in a molecule with two photons, followed by a third photon that probes the induced vibrational coherence of the molecule. Since this technique is intrinsically related to spontaneous Raman scattering, it is sensitive to the same vibrational signatures of molecules as seen in Raman spectroscopy, typically the nuclear vibrations of chemical bonds. Moreover, CRS allows imaging at video-rate speed by enhancing the weak spontaneous Raman signals which are typically 10–12 orders of magnitudes smaller than the absorption cross-sections. Coherent anti-Stokes Raman scattering (CARS) is a third-order non-linear CRS process based on the coherent driving of molecules in the focal volume, thus producing coherent radiation.[28] It has been extensively used to visualize lipids through the stretching vibrations of their carbon–hydrogen (CH) bonds[29,30] due to high Raman cross-section. In CARS, three laser beams are involved in the process: a pump beam of frequency ω_p, a Stokes beam of frequency ω_s and a probe beam at frequency ω_{pr}. In brief, when the energy difference between the pump and Stokes matches the energy gap of a particular vibrational transition the beating (difference frequency) between the pump and Stokes beams drives the vibrational oscillators within the focus coherently in phase. The resulting vibrational coherence is further read out by additional scattering of the pump beam to generate a coherent radiation at the anti-Stokes frequency, which is the basis of the technique's intrinsic vibrational contrast mechanism. No energy is deposited in the molecule during the CARS process. Instead the molecule acts as a medium for converting the frequencies of the three incoming waves into a CARS signal. CARS imaging can be performed either by narrowband (1–10 cm^{-1}) or hyperspectral imaging. In narrow band imaging the contrast arises from a particular vibrational frequency and each pixel in the image has an intensity based on the presence of molecules that have the addressed molecular mode vibration. However, this method suffers from limited chemical selectivity, because strong signals from the peak of lipids at 2860 cm^{-1} can also be generated by dense protein structures such as keratin and collagen fibers. Spectral focusing CARS method adds another dimension and allows for fast and easy switching of the vibrational excitation frequency with chirped broadband laser pulses. Each pixel reveals many spectral data points and spectral analysis based on multiple molecular vibrations can be performed pixel-wise allowing for spatial discrimination of different molecular components in the sample.[31,32] The method is not limited to lipids and can detect drug penetration in skin[33] or distribution of nucleic acids, proteins and lipids in cells related to cell division and apoptosis.[34] Furthermore, CRS has the potential to replace current standard invasive histological methods by mapping lipids, proteins and red blood cells providing contrast similar to that in the most widely used stain in histopathology.[35]

A main limitation in NLOI arises from the tight focusing condition restricting fast scanning of large areas. Hence, despite the multifaceted abilities of conventional NLOI, its ability to identify and locate morphological landmarks in 3-D and in real-

time is lacking. Overcoming the effect of motion artefacts with scanning areas in the mm^2 to cm^2 range, and penetration depths in the mm range (wide-field), calls for integration of a complementary technique into a traditional NLOI platform.

Optical coherence tomography (OCT) provides fast label-free, non-invasive and high-resolution optical sectioning of tissues through the coherence gating of light sources covering a broad bandwidth either by the means of broad emission spectra or fast sweeping. It enables spatial resolution down to microns over areas of a couple of cm^2.[36] With typical penetration depths of several millimetres, OCT reveals the intrinsic 3D structure of tissue *in situ* based on interferometry with vast applications in the medical field at video rate acquisition speeds.[36] Within two decades OCT has become the prime diagnostic imaging modality in ophthalmology[37,38] and has increased its impact in cardiology,[39] dermatology,[40,41] dentistry,[42] cancer research[43–45] and a variety of other applications. Detecting structural information on a cellular level broadens the understanding of tissue environment for *in vivo* studies, but the lacking molecular specificity hinders differentiation between pathologic and healthy tissues with similar scattering or structural properties. Structural changes of tissues and cells typically occur only after carcinogenic biochemical alterations. OCT contrast can be enhanced by different implementations,[46] *e.g.* polarization-sensitive OCT,[47] spectroscopic OCT[48] and Doppler OCT[49] as important functional variants. Nonetheless, molecular specificity on a cellular level is still limited. Hence, despite the prowess of this technology, the sensitivity and specificity to detect pathologic tissue is restricted.

To overcome the complementary limitations of NLOI and OCT a fast and non-invasive multimodal imaging platform with the capability to visualize structural, molecular and metabolic information from tissue is demanded. Both techniques, NLOI and OCT, make use of non-ionizing radiation offering the potential to asses structural, functional, metabolic and molecular features in pathophysiological conditions even during interventions in a harmless way with multiple interaction mechanisms.[50] The combination of OCT with NLOI adds inherent molecular selectivity while retaining maximum flexibility and therefore paves the way towards *in vivo* optical digital histology. Additionally, this combined approach is also suitable for other medical applications, capturing data *in vivo* and real time on a multi-dimensional scale with ultra-high sensitivity and specificity. Hence, it will expand the range of powerful non-invasive multimodal diagnostic techniques providing more information on *in vivo* tissues on the molecular, cellular and structural level and could improve their importance in a clinical context.[51]

Molecular-sensitive OCT with CARS was presented in several variants including non-linear vibrational imaging[52] with different sophisticated laser sources[53,54] and single laser source approaches.[55,56] Most of these approaches lack real-world applications due to sophisticated requirements on the sample – thin slices of transparent samples with high Raman cross-sections to be investigated in transmission or reflection mode. Also OCT and TPEF (multiphoton) were combined in various configurations[57–62] and also merged with SHG[57,63–65] or fluorescence lifetime imaging microscopy (FLIM)[66,67] showing augmented contrasts with the same field of view (FOV) and resolution for all modalities. OCT contrast and resolution was enhanced with excited second-harmonic waves from collagen harvested from rat tail tendon and a reference crystal.[54,68,69] Simultaneous cellular imaging has been reported[58,70,71] and microscopic collagen distribution and structural information have been visualized in an *in vitro* wound healing model.[72] *In vivo* skin imaging on a cellular level demonstrated the potential for diagnostic applications in dermatology.[73–75] Recent combinations of OCT and TPEF (multiphoton) with integration into endoscopes expands the range of possible applications further.[71,76–79]

All NLOI techniques are achieved only at very high photon concentration in space and time, requiring extremely high NIR laser intensities. Ultra-fast lasers provide short pulses with high peak powers required to achieve sufficient excitation powers for NLOI signal generation with moderate time-averaged illumination doses. Until recently, ultra-broadband Ti:sapphire lasers, proven and well-established light sources for multimodal NLOI in order to obtain high photon density at the focal position, have introduced high costs and complexity.[3,15,24,80,81] They emit light in the NIR wavelength region where light scattering and photo-damage effects are low and the water absorption is still acceptable, enabling tissue imaging down to more than 0.5 mm with intrinsic three-dimensional spatial resolution and high contrast. Furthermore, they provide transient intensities of GW cm^{-2} in a pulsed form with pulse durations ranging in the femtosecond regime, resulting in ultra-broad bandwidths at a peak light emission at 800 nm and repetition rates in the 70–100 MHz range. As a result, non-linear signals can be efficiently generated at average laser powers of a few mWs on the sample. Within the last decade diode pumping multiplex CARS and TPEF have been merged by applying ultra-fast Ti:sapphire lasers.[31,32,82,83] Direct diode-pumping of mode-locked Ti:sapphire lasers[84] and scaling up of the achievable output power[85] will pave the way towards more widespread application of this technology beyond scientific research. Recently, a compact and cost-effective Ti:sapphire laser was implemented in a multimodal epi-detection non-linear microscope and multiphoton system.[86,87] Due to the large bandwidth and center wavelength of 800 nm, high contrast ultra-high resolution OCT images can also be generated and therefore there is a demand for implementation of these light sources into OCT systems.[88]

In this paper, we have developed a multimodal imaging platform that incorporates OCT, spectral focusing CARS, SHG, and TPEF to collect structural and biochemical information by merging well-developed optical imaging techniques with ultrafast Ti:sapphire lasers integrated in a LSM. Since each modality measures different tissue characteristics, we predict that their combination will increase the sensitivity and specificity for detecting early tissue alteration compared to standard diagnostic methods and may provide a new insight in the diagnosis of different diseases.

Methods and experiments

One major consideration in the development of the multimodality imaging platform lies in the ability to perform fast wide-field OCT and consecutive simultaneous NLOI in the backward propagation direction without causing one modality to interfere with the others and compromising image quality. Our approach is designed on the base of a custom-modified LSM where we combine OCT with spectral focusing CARS, SHG and TPEF.

The limited penetration offered by standard microscopy techniques is overcome by OCT which allows volumetric morphological imaging for *ex vivo* and *in vivo* cell-based imaging approaches – not only surface scanning determination. Specific regions of interest (ROI) or landmarks can be identified by OCT and then correlated with label-free molecular biomarkers. Overall the integration of all modalities offers the unique opportunity to non-destructively, non-invasively and partly simultaneously analyse the morphological and molecular composition of the sample to be investigated.

Multimodal platform

Fig. 1 illustrates the principal features of our customized multimodal setup. In our system, spectral focusing CARS, TPEF, and SHG can currently be performed simultaneously after finding a structure of interest in our OCT real-time preview. The developed platform can be logically divided into several subsystems, namely the OCT engine, the NLOI engine, and the LSM for imaging. OCT and NLOI are optically and electronically synchronized such that the multimodal images are intrinsically co-registered and collected consecutively. Wide-field OCT images are recorded first and real-time preview enables localization of ROIs to be imaged with NLOI. A platform to secure the samples is situated on the top of programmable xy and z stages (PILine xy M687, PInano z P736, Physik Instrumente GmbH & Co. KG) directly beneath the objective lens. OCT and NLOI use two different sets of light sources and detectors with all acquisition channels combined into a customized upright microscope (Nikon Eclipse E400). The LSM is driven by a pair of galvanometric mirrors (6220H 8 mm, Cambridge Technology) to allow for raster scanning. NLOI and

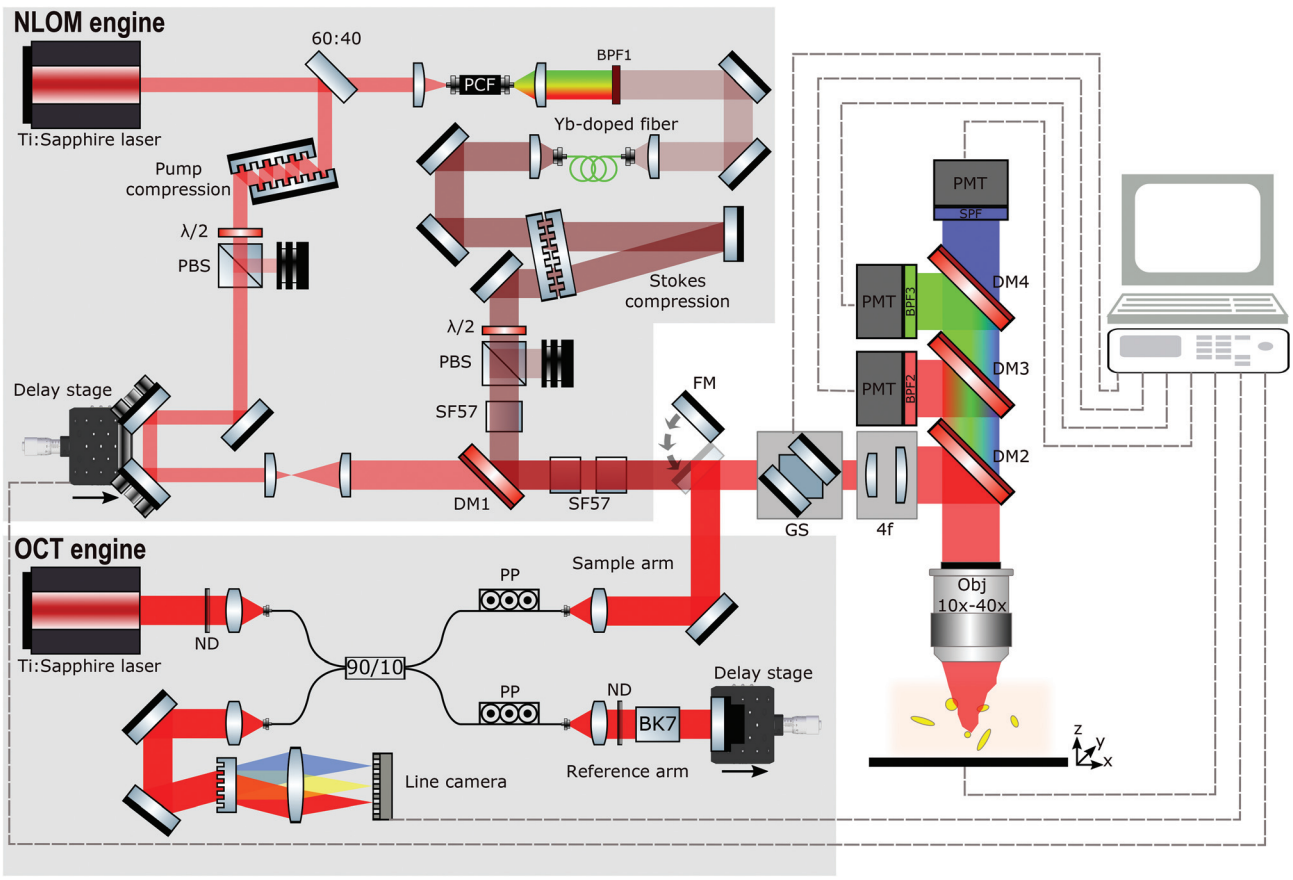

Fig. 1 Setup of the multimodal platform. Three main parts of the multimodal platform can be distinguished: the NLOI engine, the OCT engine and the common LSM imaging unit. In dashed gray lines are the electrical connections to electronically control and synchronize the collection of the excited signals. BPF: band pass filter (BPF1: 1040 nm/40 nm, BPF2: 640 nm/50 nm, BPF3: 400 nm/50 nm); SPF: 715 nm short pass filter; PBS: polarization beamsplitter; SF57: 5 cm glass block of SF57; DM: dichroic mirror; FM: flipping mirror; PP: polarization paddle; ND: neutral density filter; GS: galvanometric scanner; PMT: photomultiplier tube.

OCT utilize only one optical excitation scanning path facilitating co-registration. Light is focused on the sample by means of two different objectives to obtain reasonable lateral resolution and FOV for each modality. The different imaging modalities, OCT and NLOI can be simply switched by a flipping mirror.

OCT engine

The schematic of the spectral domain (SD) OCT engine uniting coherence gated depth information of OCT with high lateral resolution of confocal microscopy for isotropic ultra-high resolution imaging and sufficient penetration depth is shown in Fig. 1. A low-coherence, ultra-broadband compact Ti:sapphire laser centered at ~800 nm with 150 nm bandwidth at full width half maximum (FWHM) and 75 MHz repetition rate is used as a light source for SD OCT.[88,89] The laser output is focused into a single mode fiber to direct the beam into a fiber-based Michelson interferometer with a 90 : 10 single mode fiber coupler (45-U7980-20-23162, Gould Fiber Optics, USA). Two reflective fiber collimators (RC04FC-01, Thorlabs, USA) at the exits of the fiber coupler direct and collimate the light in the free space part of reference and sample arm.

Polarization paddles are used to match the polarization of the light in both arms before recombination in the detection arm. Neutral density filters (Thorlabs, NDC-50C-4) are inserted in both arms to reduce the laser power in order to not saturate the detector. In the reference arm, glass blocks composed of BK7 balance the dispersion introduced by all the optical elements present in the sample arm. At the end of the reference arm, a silver (Ag) mirror is placed on a translation stage to match the optical path length between the reference arm and the sample arm, and to couple the light back into the detection arm. In the sample arm, a mirror on a flipping mount is inserted to direct the light from the SD OCT engine into the microscope and focus on the sample with a 10× objective (Nikon CFI Achro 10× 0.25NA). The backscattered light from the sample is de-scanned by propagating backwards through the 4f system and galvanometric scanning mirrors, recollected by the fiber collimator, recombined with light from the reference arm and directed to the detection arm with a spectrometer supporting a bandwidth of 260 nm. The collimated light (collimator focal length f = 100 mm, OZ, Ottawa, Canada) is sent through the 1200 lines per mm grating (Wasatch Photonics, Logan, USA) with 840 nm central wavelength. Then the diffracted light is focused with an f = 85 mm objective (ZEISS PLANAR T 1.4/85 ZF-IR-I, Carl Zeiss, Oberkochen, Germany) onto the 2048 pixels of the 12-bit CCD line scan camera with 70 kHz maximum line-rate (AViiVA Atmel EM4CL 2014, Essex, UK). The spectrometer acquires 2048 samples for each A-scan at a measured rate of 67 kHz and is calibrated with an external commercial spectrometer. The maximum depth samples are around 1.3 mm in free space, approximately corresponding to 1.3 μm depth resolution. The axial resolution achievable by the imaging system is 2.1 μm in air corresponding to ~1.4 μm in tissue and is almost constant over the whole depth range with a 9 dB signal roll-off over 1 mm. The sensitivity is measured as 96 dB in tissue including the losses in the microscope (50% single pass). In the experimental set-up a lateral resolution better than 2.19 μm can be measured with an USAF 1951 Resolution Target. The SD OCT system is set-up to acquire volumes consisting of 400 B-Scans with 400 A-Scans/B-Scan and 2048 pixels/A-Scan. From 2048 pixels/A-Scan, only 1024 pixels are usable to extract the depth profile due to the complex-conjugate artefact. The maximum volume size in one acquisition is 1.2 mm × 1.2 mm × 1.3 mm. The acquisition speed of 166 B-Scans per s gives the total time of 2.4 s to acquire one volume. The maximum incident power at the samples is 2.5 mW. Data acquisition is performed using a PC with a NI PCIe-1430 frame-grabber and controlled using a NI PCI-6115 data acquisition card (National Instruments) with a custom software written in MATLAB. Only one PC is required to operate the data acquisition control boards in the microscope for OCT and NLOI. Real-time preview facilitates the identification of ROIs and controls the zoom into specific regions with high resolution and molecular specificity.

NLOI engine

In brief, the integrated spectral focusing CARS, SHG and TPEF imaging platform is based on two-color excitation beams and three detection channels as described in detail elsewhere.[86] In our previous work on the development of a compact epi-directed non-linear imaging device several unique strategies were implemented to seamlessly and simultaneously acquire hyperspectral CARS, SHG and TPEF signals within the focal volume in the epi-direction. These strategies included the implementation of a compact and cost-effective Ti:sapphire laser centered at ~805 nm with 15 nm bandwidth at FWHM compressed to ~70 fs and 75 MHz repetition rate used as pump beam for CARS and to excite TPEF and SHG. It is also used to pump a polarization-maintaining photonic crystal fiber (PCF) whose filtered output is further amplified with a Yb:fiber amplifier to generate the Stokes beam used in CARS centered at 1050 nm with 18 nm bandwidth at FWHM and compressed to ~100 fs generated by the Ti:sapphire laser as shown in Fig. 1. Spectral focusing CARS (adding a spectral dimension to CARS images) is realized by introducing equal chirp on pump and Stokes pulses with the insertion of SF57 glass blocks[31,32,83] enabling a spectral resolution for CARS spectroscopy of about ~35 cm^{-1}. The change of the temporal overlap controlled by a computer-controlled delay stage allows for fast tuning of Raman frequencies corresponding to the CH stretching vibrations. Pump and Stokes beams are recombined with a dichroic beamsplitter, directed into the LSM and focused on the sample (NIR Apo 40× Nikon). Epi-detected signals from CARS, TPEF and SHG are collected in a non-descanned geometry by the objective and discriminated from the excitation signal by means of a dichroic mirror immediately above the objective. In addition, the excited light signals are guided to an array of photomultiplier tubes using a lens, dichroic mirror and detection filters. The detector consisting of three channels covers the range of CARS, SHG, and

TPEF signals (Channel 1: 640 nm ± 25 nm, Channel 2: 400 nm ± 25 nm, and Channel 3: 512 nm ± 100 nm). ScanImage 3.8 software[90] controls the galvanometer scanners and data acquisition in combination with the custom Matlab program to ensure impeccable communication between the programs and different modalities.

Results and discussion

The performance of the label-free multimodal optical imaging platform is demonstrated by recording OCT and NLOI images of a portion of freshly excised mouse ear tissue within less than one hour after excision. We use a real-time preview to located different ROIs and acquire OCT volumes with a size of $1.2 \times 1.2 \times 1.3$ mm^3 within 2.4 s. OCT provides en face images to visualize the topology of the mouse ear and OCT cross-sections to obtain the capability to differentiate between the different layers the skin, the epidermis and dermis with the epidermis junction as shown in Fig. 2. The orthogonal views of the skin reveal the epidermis (E), which is the surface of the skin, at the very top. Underneath the epidermis, the dermis junction can be seen, followed by the dermis (D) where hair follicles with follicle shaft and the follicle bulb as well as sebaceous glands (SG) and small blood and lymph vessels are located. The dark layer inside the tissue is the auricular cartilage (AC) of the ear followed by adipose tissue (AT). Sebaceous glands can be identified within the dermis layer, 50 μm below the epidermis as indicated in Fig. 2 by the yellow cross-hairs. The cross-hairs in the orthogonal views indicate the position of our ROI (the sebaceous gland) where the NLOI is performed. As outlined before, OCT and NLOI have different FOVs. The three dimensional topological overview obtained by wide-field screening with OCT allows for zooming into specific ROIs with

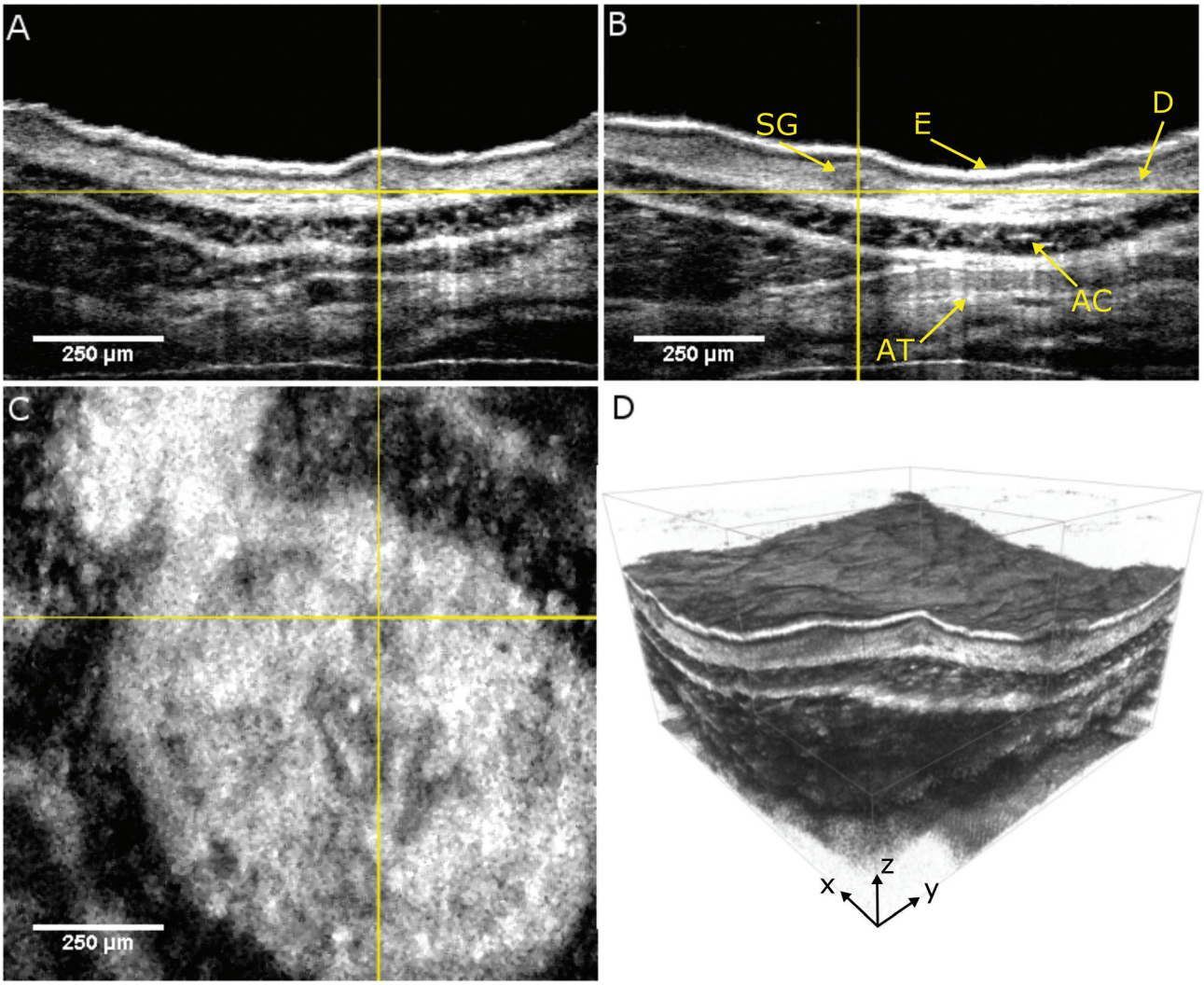

Fig. 2 OCT orthogonal views of freshly excised mouse ear tissue allowing identification of epidermis (E), dermis (D), sebaceous gland (SG), auricular cartilage (AC) and adipose tissue (AT). Panel A, B and C are 2D views of the volumetric information in panel D used to localize a single sebaceous gland (yellow cross-hairs): panel A represents *xz* plane, panel B *yz* plane and panel C *xy* plane. In (D) we show the 3D visualization of the mouse ear tissue with a volume cut corresponding to the plane in panel (A), (B) and (C). Pixel aspect ratio 1 : 1 : 1.

simultaneous collection of SHG, TPEF, and CARS signals in the CH stretching region.

Hence, we zoom into the specific sebaceous gland positioned in the center of the cross-hairs in Fig. 2 and investigate our biological tissue of interest on a biochemical level. There is a growing interest in its physiology which can be assessed by looking at the lipid content of the cells forming the gland due to its complex neuro-immune endocrine functions[91,92] and several medical conditions in humans involving sebum.[92,93]

The multimodal NLOI images in Fig. 3 were taken 50 μm deep in the tissue with a FOV of 256 × 256 pixels corresponding to 70 × 70 μm and with 6.4 μs pixel dwell time. A compromise between image quality and acquisition speed, depending on the strength of the excited signal has been made in this case. NLOI is capable of visualizing the bright structures surrounding the follicle in the second layer of the skin, the sebaceous glands. Due to its CH bonding and high Raman cross section, fatty components can be easily visualized with CARS. Hence, the sebocytes forming the sebaceous gland can be perfectly visualized in the CARS channel due to their high lipid content shown in Fig. 3C (red color-coded). They are multicellular compartments packed with sebum reservoirs containing triglycerides and wax esters. Intracellular lipid lobuli inside each sebocyte forming the sebaceous gland are clearly visible as bright granuli due to their high lipid content. Nuclei marked with N and cell membranes marked with M appear as dark structures due to their poor lipid content. Also, the hair shaft marked with F can be visualized. The contrast in the CARS image in Fig. 3 arises from the Raman resonance located at 2860 cm^{-1} with an indicated spectral resolution of 35 cm^{-1}. Additional contrast from collagen and elastin can be revealed in SHG and TPEF channels as shown in Fig. 3A and B. The ECM in the dermis providing structural and biochemical support for the sebaceous gland mainly consists of collagen fibers, accompanied by reticular and elastic fibers. While collagen fibers generate SHG signal detected in channel 2 (blue color-coded), elastin fibers generate strong autofluorescence as visible in channel 3 (green color-coded). Also, the signal from the hair follicle, especially from the hair shaft (F) is visible through its elastin, keratin and lipid content appears in the TPEF and CARS channels. Fig. 3D shows a merged multimodal image of the sebaceous gland. The epi-detected CARS, SHG, and TPEF images are represented with red, blue, and green, respectively. All images are obtained with a frame rate of about 1 Hz. The pump and Stokes powers are 19 and 6 mW on the sample, respectively. As already reported sebaceous glands and subcutaneous fat cells have different lipid compositions which can be probed at different locations in the CH stretching region (2800–3100 cm^{-1}). This variance indicates the difference between highly saturated lipids in the gland and the mono-unsaturated lipid acyl chain in the adipocytes. Since our CARS signals are generated by means of chirped pulses (spectral focusing) a spectral dimension is added to the CARS image providing molecule-specific information of the tissue for better interpretation of images where heterogeneous molecular composition aggravates the analysis and discrimination, *e.g.* between protein and lipids. The spectroscopic capability of the system is demonstrated by recording hyperspectral images. A projection of a 120 image dataset from the mouse ear is recorded along the spectral range from ~2550 to 3200 cm^{-1}, corresponding to a time delay between the pump and Stokes pulses of ~1.5 ps. Fig. 4A represents the spectral profile of a single lipid droplet within the sebaceous gland, identified by the OCT engine, embedded 50 μm in mouse ear tissue. Two red dotted lines indicate two different Raman shifts, 2760 cm^{-1} and 2860 cm^{-1}, respectively. The images in Fig. 4C and D are acquired at these Raman shifts. Thus, our platform is not only capable of spatial discrimination, but also spectral discrimination. The Raman shift at 2860 cm^{-1} in Fig. 4D visualizes structures based on intrinsic vibrational properties without staining or labelling the specimen and reveal the lipid distribution in the CH stretching region, while the Raman shift at 2760 cm^{-1} shows the off resonant contribution of the sebaceous gland and enhances the surrounding medium as visualized in Fig. 4C. The intensity profiles (red and blue) shown in Fig. 4B correspond to the yellow dotted lines in the on (Fig. 4D) and off (Fig. 4C) resonant images and reveal the local distribution of the lipid droplets, on and off resonance, within the sebocytes. Especially the red profile reveals the location of lipid droplets (LDs) within the sebocytes, the cell membrane (M), nuclei (N) and hair shaft (F).

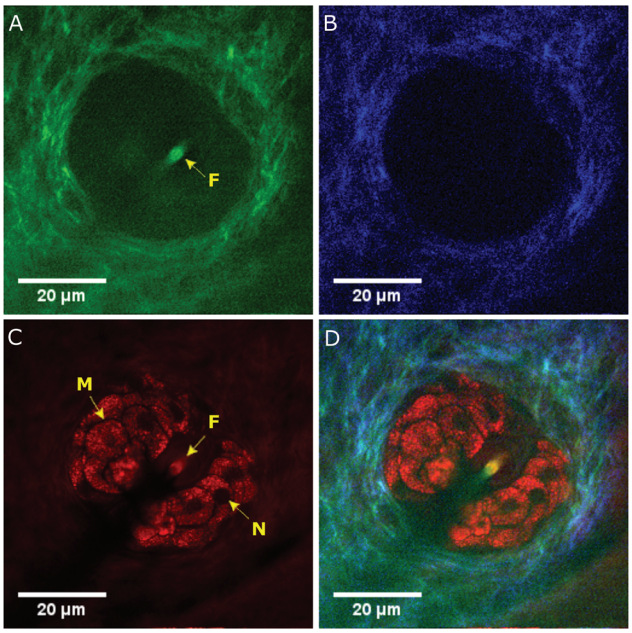

Fig. 3 Epi-detected multimodal NLOI images of a sebaceous gland. (A) Elastin and (B) collagen content of the ECM supporting the gland visualized through TPEF and SHG, respectively; (C) lipid content of the gland imaged by CARS where it is possible to identify the sebocytes' membranes (M) and nuclei (N) and as well the location of the follicle (F). (D) Merged image of (A), (B) and (C) showing the complementary information provided by TPEF, SHG and CARS.

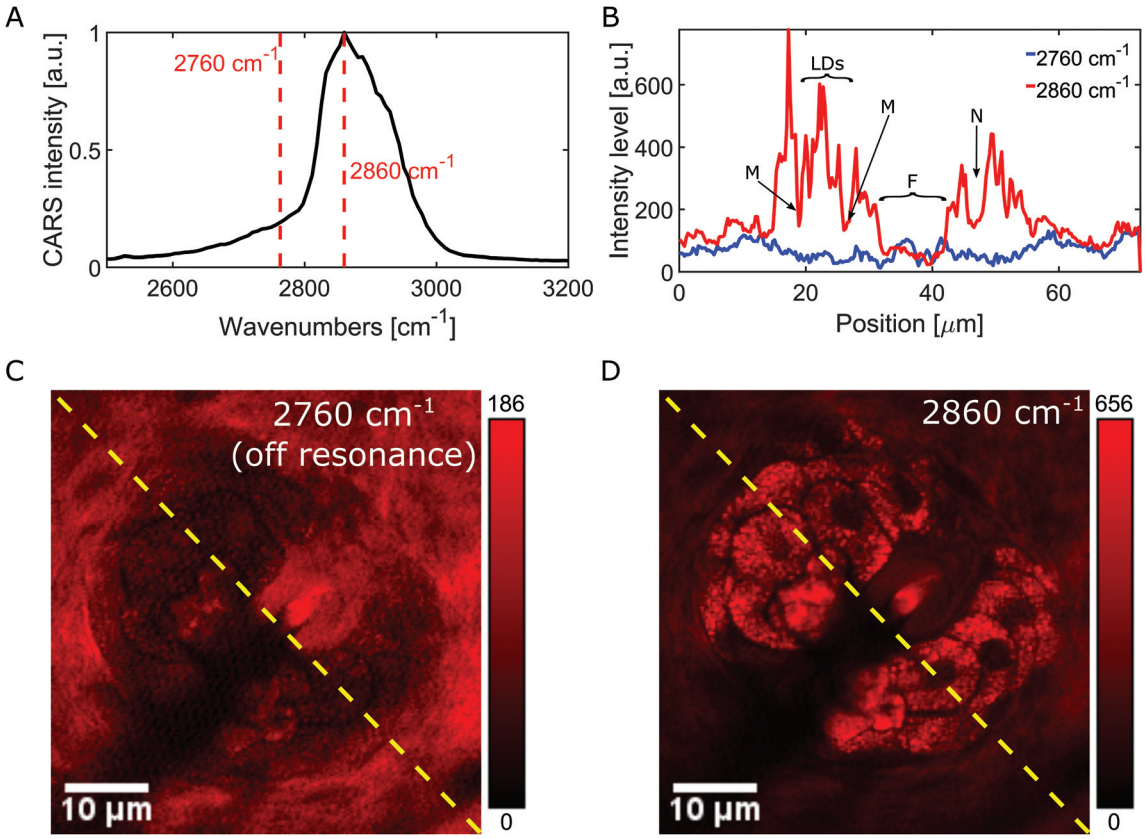

Fig. 4 Contrast equalized hyperspectral CARS images of a sebaceous gland identified by the OCT engine 50 μm deep into tissue at different Raman shifts. (A) Spectral profile of a single lipid droplet within a sebocyte. The hyperspectral scan is superimposed by the location of two specific shifts (2760 cm^{-1} (off resonance), 2860 cm^{-1} (on resonance)) indicated with red dotted lines. (B) The intensity profiles (red (on resonance), and blue (off resonance)) correspond to the yellow dotted lines in (C) and (D) revealing the local distribution of the cell membranes (M), nuclei (N), lipid droplets (LDs) and hair shafts (F). (C) Off resonance image at a Raman shift of 2760 cm^{-1} highlighting the sebaceous gland surrounding structure. (D) On resonance image at a Raman shift of 2860 cm^{-1} highlighting the lipid content within the sebaceous gland.

Conclusions

An epi-detected hyperspectral microscope based on an ultrafast Ti:sapphire laser is an ideal platform providing structural, molecular and biochemical information with high sensitivity and specificity. In biomedical imaging applications, however, imaging speed is also very important. As we demonstrate in this work, the integration of OCT and NLOI into a LSM with ultrafast Ti:sapphire lasers provides fast structural ultra-high resolution wide-field pre-screening to localize specific ROIs and zoom into the structure, function and metabolism of biological tissue on a cellular level with high contrast in a non-contact and non-destructive endogenous manner where no stains are required to enhance the contrast. Hence, the specimen does not suffer from perturbation by dye or photo-bleaching.

Current limited penetration offered by standard microscopy techniques is overcome with OCT allowing for deeper tissue interrogation for *in situ* cell-based imaging approaches and not only surface scanning determination. Particularly interesting areas can be correlated with label-free molecular biomarkers that can be instantaneously interpreted. TPEF, SHG and spectral focusing CARS imaging is integrated into a LSM and OCT is added to obtain complementary structural and functional information within tissue samples and cells. The potential of the platform is demonstrated in an established animal model. One significant difference compared with previous combined methods is that this device intrinsically has the multi-functionalities of OCT and OCM adding highly specific molecular and spectroscopic information with spectral focusing CARS on a cellular level. Overall integration of all the complementary modalities offers the opportunity to non-destructively and partly simultaneously investigate the structure, molecular distribution and function of biological tissue in three dimensions and in real-time with isotropic micron-scale resolution in a label-free manner. The current limitations of our systems are that the co-localisation is done only optically, there is no registration based feedback system, and that the flipping mirror prevents simultaneous acquisition of OCT and NLOI. These drawbacks can be overcome by integration of an automatic feedback system interfacing the stage and scanner control as well as the implementation of a beam combiner. Hence, our platform can potentially address a wide variety of unmet clinical needs for disease detection and localization by providing a wealth of intrinsic molecular and mor-

phological information quickly and with high sensitivity and specificity. Due to the modular concept, our proposed system can also be interfaced to commercial LSM systems and could be used in conjunction with super-resolution methods including structured illumination or Airyscan. We hope that our contribution is a step further to shift the current gold standard of histopathology and adopt a new paradigm of *in vivo* molecular histopathology – truly enacting the concept of optical biopsy.

Conflicts of interest

There are no conflicts to declare.

Acknowledgements

This work was supported by the European Union's Horizon 2020 research and innovation programme (MIB H2020-PHC-2015-two-stage and MOON H2020-ICT-2016-1) under grant agreement No. 667933 and 732969. The author M. T. E. has received funding from the European Union's Horizon 2020 research and innovation programme under the Marie Skłodowska-Curie grant agreement No. 721766. The authors acknowledge the contribution of Tuan Le from Medical University of Vienna for technical assistance with the light sources.

Notes and references

1 B. C. Wilson, M. Jermyn and F. Leblond, Challenges and opportunities in clinical translation of biomedical optical spectroscopy and imaging, *J. Biomed. Opt.*, 2018, **23**, 030901.
2 S. Yue, M. N. Slipchenko and J.-X. Cheng, Multimodal nonlinear optical microscopy, *Laser Photonics Rev.*, 2011, **5**, 496–512.
3 C. P. Pfeffer, B. R. Olsen, F. Ganikhanov and F. Légaré, Multimodal nonlinear optical imaging of collagen arrays, *J. Struct. Biol.*, 2008, **164**, 140–145.
4 A. Zoumi, A. Yeh and B. J. Tromberg, Imaging cells and extracellular matrix in vivo by using second-harmonic generation and two-photon excited fluorescence, *Proc. Natl. Acad. Sci. U. S. A.*, 2002, **99**, 11014–11019.
5 W. R. Zipfel, R. M. Williams and W. W. Webb, Nonlinear magic: multiphoton microscopy in the biosciences, *Nat. Biotechnol.*, 2003, **21**, 1369–1377.
6 F. Helmchen and W. Denk, Deep tissue two-photon microscopy, *Nat. Methods*, 2005, **2**, 932–940.
7 C. L. Evans, E. O. Potma, M. Puoris'haag, D. Cote, C. P. Lin and X. S. Xie, Chemical imaging of tissue in vivo with video-rate coherent anti-Stokes Raman scattering microscopy, *Proc. Natl. Acad. Sci. U. S. A.*, 2005, **102**, 16807–16812.
8 M. Ji, S. Lewis, S. Camelo-Piragua, S. H. Ramkissoon, M. Snuderl, S. Venneti, A. Fisher-Hubbard, M. Garrard, D. Fu, A. C. Wang, J. A. Heth, C. O. Maher, N. Sanai, T. D. Johnson, C. W. Freudiger, O. Sagher, X. S. Xie and D. A. Orringer, Detection of human brain tumor infiltration with quantitative stimulated Raman scattering microscopy, *Sci. Transl. Med.*, 2015, **7**, 309ra163–309ra163.
9 D. R. Rivera, C. M. Brown, D. G. Ouzounov, I. Pavlova, D. Kobat, W. W. Webb and C. Xu, Compact and flexible raster scanning multiphoton endoscope capable of imaging unstained tissue, *Proc. Natl. Acad. Sci. U. S. A.*, 2011, **108**, 17598–17603.
10 J. Hou, J. Williams, E. L. Botvinick, E. O. Potma and B. J. Tromberg, Visualization of Breast Cancer Metabolism Using Multimodal Nonlinear Optical Microscopy of Cellular Lipids and Redox State, *Cancer Res.*, 2018, **78**, 2503–2512.
11 W. Denk, J. H. Strickler and W. W. Webb, Two-photon laser scanning fluorescence microscopy, *Science*, 1990, **248**, 73–76.
12 W. Y. Sanchez, T. W. Prow, W. H. Sanchez, J. Grice and M. S. Roberts, Analysis of the metabolic deterioration of ex vivo skin from ischemic necrosis through the imaging of intracellular NAD(P)H by multiphoton tomography and fluorescence lifetime imaging microscopy, *J. Biomed. Opt.*, 2010, **15**, 046008.
13 M. Balu, A. Mazhar, C. K. Hayakawa, R. Mittal, T. B. Krasieva, K. König, V. Venugopalan and B. J. Tromberg, In vivo multiphoton NADH fluorescence reveals depth-dependent keratinocyte metabolism in human skin, *Biophys. J.*, 2013, **104**, 258–267.
14 G. Thomas, J. van Voskuilen, H. C. Gerritsen and H. J. Sterenborg, Advances and challenges in label-free nonlinear optical imaging using two-photon excitation fluorescence and second harmonic generation for cancer research, *J. Photochem. Photobiol., B*, 2014, **141**, 128–138.
15 W. R. Zipfel, R. M. Williams, R. Christie, A. Y. Nikitin, B. T. Hyman and W. W. Webb, Live tissue intrinsic emission microscopy using multiphoton-excited native fluorescence and second harmonic generation, *Proc. Natl. Acad. Sci. U. S. A.*, 2003, **100**, 7075–7080.
16 K. Vishwanath and N. Ramanujam, in *Encyclopedia of Analytical Chemistry*, American Cancer Society, 2011.
17 B.-G. Wang, K. König and K.-J. Halbhuber, Two-photon microscopy of deep intravital tissues and its merits in clinical research, *J. Microsc.*, 2010, **238**, 1–20.
18 M. Y. Berezin and S. Achilefu, Fluorescence lifetime measurements and biological imaging, *Chem. Rev.*, 2010, **110**, 2641–2684.
19 E. Brown, T. McKee, E. diTomaso, A. Pluen, B. Seed, Y. Boucher and R. K. Jain, Dynamic imaging of collagen and its modulation in tumors in vivo using second-harmonic generation, *Nat. Med.*, 2003, **9**, 796–800.
20 F. S. Pavone and P. J. Campagnola, *Second Harmonic Generation Imaging*, CRC Press, 2013.
21 I. Freund, M. Deutsch and A. Sprecher, Connective tissue polarity. Optical second-harmonic microscopy, crossed-beam summation, and small-angle scattering in rat-tail tendon, *Biophys. J.*, 1986, **50**, 693–712.

22 M. Nuriya, J. Jiang, B. Nemet, K. B. Eisenthal and R. Yuste, Imaging membrane potential in dendritic spines, *Proc. Natl. Acad. Sci. U. S. A.*, 2006, **103**, 786–790.
23 O. Nadiarnykh, R. B. LaComb, M. A. Brewer and P. J. Campagnola, Alterations of the extracellular matrix in ovarian cancer studied by Second Harmonic Generation imaging microscopy, *BMC Cancer*, 2010, **10**, 94.
24 J. Sun, T. Shilagard, B. Bell, M. Motamedi and G. Vargas, In vivo multimodal nonlinear optical imaging of mucosal tissue, *Opt. Express*, 2004, **12**, 2478–2486.
25 E. J. Gualda, G. Filippidis, G. Voglis, M. Mari, C. Fotakis and N. Tavernarakis, In vivo imaging of cellular structures in Caenorhabditis elegans by combined TPEF, SHG and THG microscopy, *J. Microsc.*, 2008, **229**, 141–150.
26 J. N. Rogart, J. Nagata, C. S. Loeser, R. D. Roorda, H. Aslanian, M. E. Robert, W. R. Zipfel and M. H. Nathanson, Multiphoton Imaging Can Be Used for Microscopic Examination of Intact Human Gastrointestinal Mucosa Ex Vivo, *Clin. Gastroenterol. Hepatol.*, 2008, **6**, 95–101.
27 J. Yan, G. Chen, J. Chen, N. Liu, S. Zhuo, H. Yu and M. Ying, A pilot study of using multiphoton microscopy to diagnose gastric cancer, *Surg. Endosc.*, 2011, **25**, 1425–1430.
28 M. D. Duncan, J. Reintjes and T. J. Manuccia, Scanning coherent anti-Stokes Raman microscope, *Opt. Lett.*, 1982, **7**, 350–352.
29 S.-H. Kim, E.-S. Lee, J. Y. Lee, E. S. Lee, B.-S. Lee, J. E. Park and D. W. Moon, Multiplex coherent anti-stokes Raman spectroscopy images intact atheromatous lesions and concomitantly identifies distinct chemical profiles of atherosclerotic lipids, *Circ. Res.*, 2010, **106**, 1332–1341.
30 T. B. Huff, Y. Shi, Y. Fu, H. Wang and J.-X. Cheng, Multimodal Nonlinear Optical Microscopy and Applications to Central Nervous System Imaging, *IEEE J. Sel. Top. Quantum Electron.*, 2008, **14**, 4–9.
31 A. F. Pegoraro, A. Ridsdale, D. J. Moffatt, Y. Jia, J. P. Pezacki and A. Stolow, Optimally chirped multimodal CARS microscopy based on a single Ti:sapphire oscillator, *Opt. Express*, 2009, **17**, 2984–2996.
32 T. Hellerer, A. M. K. Enejder and A. Zumbusch, Spectral focusing: High spectral resolution spectroscopy with broadbandwidth laser pulses, *Appl. Phys. Lett.*, 2004, **85**, 25.
33 B. G. Saar, L. R. Contreras-Rojas, X. S. Xie and R. H. Guy, Imaging Drug Delivery to Skin with Stimulated Raman Scattering Microscopy, *Mol. Pharmaceutics*, 2011, **8**, 969–975.
34 X. Zhang, M. B. J. Roeffaers, S. Basu, J. R. Daniele, D. Fu, C. W. Freudiger, G. R. Holtom and X. S. Xie, Label-free live-cell imaging of nucleic acids using stimulated Raman scattering microscopy, *ChemPhysChem*, 2012, **13**, 1054–1059.
35 C. W. Freudiger, R. Pfannl, D. A. Orringer, B. G. Saar, M. Ji, Q. Zeng, L. Ottoboni, Y. Wei, W. Ying, C. Waeber, J. R. Sims, P. L. De Jager, O. Sagher, M. A. Philbert, X. Xu, S. Kesari, X. S. Xie and G. S. Young, Multicolored stain-free histopathology with coherent Raman imaging, *Lab. Invest.*, 2012, **92**, 1492–1502.
36 D. Huang, E. A. Swanson, C. P. Lin, J. S. Schuman, W. G. Stinson, W. Chang, M. R. Hee, T. Flotte, K. Gregory, C. A. Puliafito and J. G. Fujimoto, Optical Coherence Tomography, *Science*, 1991, **254**, 1178–1181.
37 W. Drexler, U. Morgner, R. K. Ghanta, F. X. Kärtner, J. S. Schuman and J. G. Fujimoto, Ultrahigh-resolution ophthalmic optical coherence tomography, *Nat. Med.*, 2001, **7**, 502–507.
38 W. Drexler, H. Sattmann, B. Hermann, T. H. Ko, M. Stur, A. Unterhuber, C. Scholda, O. Findl, M. Wirtitsch, J. G. Fujimoto and A. F. Fercher, Enhanced visualization of macular pathology with the use of ultrahigh-resolution optical coherence tomography, *Arch. Ophthalmol.*, 2003, **121**, 695–706.
39 L. Vignali, E. Solinas and E. Emanuele, Research and clinical applications of optical coherence tomography in invasive cardiology: a review, *Curr. Cardiol. Rev.*, 2014, **10**, 369–376.
40 J. Welzel, Optical coherence tomography in dermatology: a review, *Skin Res. Technol.*, 2001, **7**, 1–9.
41 M. Mogensen, L. Thrane, T. M. Jørgensen, P. E. Andersen and G. B. E. Jemec, OCT imaging of skin cancer and other dermatological diseases, *J. Biophotonics*, 2009, **2**, 442–451.
42 R. A. Katkar, S. A. Tadinada, B. T. Amaechi and D. Fried, Optical Coherence Tomography, *Dent. Clin. North Am.*, 2018, **62**, 421–434.
43 B. J. Vakoc, R. M. Lanning, J. A. Tyrrell, T. P. Padera, L. A. Bartlett, T. Stylianopoulos, L. L. Munn, G. J. Tearney, D. Fukumura, R. K. Jain and B. E. Bouma, Three-dimensional microscopy of the tumor microenvironment *in vivo* using optical frequency domain imaging, *Nat. Med.*, 2009, **15**, 1219–1223.
44 B. J. Vakoc, D. Fukumura, R. K. Jain and B. E. Bouma, Cancer imaging by optical coherence tomography: preclinical progress and clinical potential, *Nat. Rev. Cancer*, 2012, **12**, 363–368.
45 C. Kut, K. L. Chaichana, J. Xi, S. M. Raza, X. Ye, E. R. McVeigh, F. J. Rodriguez, A. Quiñones-Hinojosa and X. Li, Detection of human brain cancer infiltration ex vivo and in vivo using quantitative optical coherence tomography, *Sci. Transl. Med.*, 2015, **7**, 292ra100.
46 *Optical Coherence Tomography: Technology and Applications*, ed. W. Drexler and J. G. Fujimoto, Springer International Publishing, 2nd edn, 2015.
47 M. R. Hee, E. A. Swanson, J. G. Fujimoto and D. Huang, Polarization-sensitive low-coherence reflectometer for birefringence characterization and ranging, *J. Opt. Soc. Am. B*, 1992, **9**, 903.
48 U. Morgner, W. Drexler, F. X. Kärtner, X. D. Li, C. Pitris, E. P. Ippen and J. G. Fujimoto, Spectroscopic optical coherence tomography, *Opt. Lett.*, 2000, **25**, 111.
49 Z. Chen, T. E. Milner, S. Srinivas, X. Wang, A. Malekafzali, M. J. C. van Gemert and J. S. Nelson, Noninvasive imaging of in vivo blood flow velocity using optical Doppler tomography, *Opt. Lett.*, 1997, **22**, 1119.
50 H. Tu, Y. Liu, D. Turchinovich, M. Marjanovic, J. K. Lyngsø, J. Lægsgaard, E. J. Chaney, Y. Zhao, S. You, W. L. Wilson,

B. Xu, M. Dantus and S. A. Boppart, Stain-free histopathology by programmable supercontinuum pulses, *Nat. Photonics*, 2016, **10**, 534–540.

51 W. Drexler, M. Liu, A. Kumar, T. Kamali, A. Unterhuber and R. A. Leitgeb, Optical coherence tomography today: speed, contrast, and multimodality, *J. Biomed. Opt.*, 2014, **19**, 071412.

52 D. L. Marks and S. A. Boppart, Nonlinear Interferometric Vibrational Imaging, *Phys. Rev. Lett.*, 2004, **92**, 123905.

53 J. S. Bredfeldt, C. Vinegoni, D. L. Marks and S. A. Boppart, Molecularly sensitive optical coherence tomography, *Opt. Lett.*, 2005, **30**, 495–497.

54 C. Vinegoni, J. Bredfeldt, D. Marks and S. Boppart, Nonlinear optical contrast enhancement for optical coherence tomography, *Opt. Express*, 2004, **12**, 331–341.

55 T. Kamali, B. Považay, S. Kumar, Y. Silberberg, B. Hermann, R. Werkmeister, W. Drexler and A. Unterhuber, Hybrid single-source online Fourier transform coherent anti-Stokes Raman scattering/optical coherence tomography, *Opt. Lett.*, 2014, **39**, 5709.

56 S. Kumar, T. Kamali, J. M. Levitte, O. Katz, B. Hermann, R. Werkmeister, B. Považay, W. Drexler, A. Unterhuber and Y. Silberberg, Single-pulse CARS based multimodal nonlinear optical microscope for bioimaging, *Opt. Express*, 2015, **23**, 13082.

57 C. Vinegoni, T. Ralston, W. Tan, W. Luo, D. L. Marks and S. A. Boppart, Integrated structural and functional optical imaging combining spectral-domain optical coherence and multiphoton microscopy, *Appl. Phys. Lett.*, 2006, **88**, 053901.

58 B. W. Graf and S. A. Boppart, Multimodal In Vivo Skin Imaging with Integrated Optical Coherence and Multiphoton Microscopy, *IEEE J. Sel. Top. Quantum Electron.*, 2012, **18**(4), 1280–1286.

59 E. Beaurepaire, L. Moreaux, F. Amblard and J. Mertz, Combined scanning optical coherence and two-photon-excited fluorescence microscopy, *Opt. Lett.*, 1999, **24**, 969–971.

60 S. Tang, T. B. Krasieva, Z. Chen and B. J. Tromberg, Combined multiphoton microscopy and optical coherence tomography using a 12-fs broadband source, *J. Biomed. Opt.*, 2006, **11**, 020502.

61 S. Yuan, C. A. Roney, J. Wierwille, C.-W. Chen, B. Xu, J. Jiang, H. Ma, A. Cable, R. M. Summers and Y. Chen, Combining Optical Coherence Tomography with Fluorescence Molecular Imaging: Towards Simultaneous Morphology and Molecular Imaging, *Phys. Med. Biol.*, 2010, **55**, 191–206.

62 J. Xi, Y. Chen, Y. Zhang, K. Murari, M.-J. Li and X. Li, Integrated multimodal endomicroscopy platform for simultaneous en face optical coherence and two-photon fluorescence imaging, *Opt. Lett.*, 2012, **37**, 362–364.

63 S. P. Chong, T. Lai, Y. Zhou and S. Tang, Tri-modal microscopy with multiphoton and optical coherence microscopy/tomography for multi-scale and multi-contrast imaging, *Biomed. Opt. Express*, 2013, **4**, 1584–1594.

64 Q. Wu, B. E. Applegate and A. T. Yeh, Cornea microstructure and mechanical responses measured with nonlinear optical and optical coherence microscopy using sub-10-fs pulses, *Biomed. Opt. Express*, 2011, **2**, 1135–1146.

65 S. Yazdanfar, Y. Yu Chen, P. T. C. So and L. H. Laiho, Multifunctional Imaging of Endogenous Contrast by Simultaneous Nonlinear and Optical Coherence Microscopy of Thick Tissues, *Microsc. Res. Tech.*, 2007, **70**, 628–633.

66 A. V. Meleshina, O. S. Rogovaya, V. V. Dudenkova, M. A. Sirotkina, M. M. Lukina, A. S. Bystrova, V. G. Krut, D. S. Kuznetsova, E. P. Kalabusheva, A. V. Vasiliev, E. A. Vorotelyak and E. V. Zagaynova, Multimodal label-free imaging of living dermal equivalents including dermal papilla cells, *Stem Cell Res. Ther.*, 2018, **9**, 84.

67 Y. Zhao, B. W. Graf, E. J. Chaney, Z. Mahmassani, E. Antoniadou, R. Devolder, H. Kong, M. D. Boppart and S. A. Boppart, Integrated multimodal optical microscopy for structural and functional imaging of engineered and natural skin, *J. Biophotonics*, 2012, **5**(5–6), 437–448.

68 Y. Jiang, I. Tomov, Y. Wang and Z. Chen, Second-harmonic optical coherence tomography, *Opt. Lett.*, 2004, **29**, 1090–1092.

69 B. E. Applegate, C. Yang, A. M. Rollins and J. A. Izatt, Polarization-resolved second-harmonic-generation optical coherence tomography in collagen, *Opt. Lett.*, 2004, **29**, 2252–2254.

70 B. W. Graf, Z. Jiang, H. Tu and S. A. Boppart, Dual-spectrum laser source based on fiber continuum generation for integrated optical coherence and multiphoton microscopy, *J. Biomed. Opt.*, 2009, **14**, 034019.

71 B. Jeong, B. Lee, M. S. Jang, H. Nam, S. J. Yoon, T. Wang, J. Doh, B.-G. Yang, M. H. Jang and K. H. Kim, Combined two-photon microscopy and optical coherence tomography using individually optimized sources, *Opt. Express*, 2011, **19**, 13089–13096.

72 A. T. Yeh, B. Kao, W. G. Jung, Z. Chen, J. S. Nelson and B. J. Tromberg, Imaging wound healing using optical coherence tomography and multiphoton microscopy in an in vitro skin-equivalent tissue model, *J. Biomed. Opt.*, 2004, **9**, 248–253.

73 K. König, M. Speicher, R. Bückle, J. Reckfort, G. McKenzie, J. Welzel, M. J. Koehler, P. Elsner and M. Kaatz, Clinical optical coherence tomography combined with multiphoton tomography of patients with skin diseases, *J. Biophotonics*, 2009, **2**, 389–397.

74 K. König, Hybrid multiphoton multimodal tomography of in vivo human skin, *IntraVital*, 2012, **1**, 11–26.

75 A. Alex, J. Weingast, M. Weinigel, M. Kellner-Höfer, R. Nemecek, M. Binder, H. Pehamberger, K. König and W. Drexler, Three-dimensional multiphoton/optical coherence tomography for diagnostic applications in dermatology, *J. Biophotonics*, 2013, **6**, 352–362.

76 J. Liu, H. Xie, Z. Yuan, Z. Wang, C. S. D. Lee, W. C. Waltzer and Y. Pan, In vivo bladder imaging with micro-electromechanical-systems-based endoscopic spectral domain optical coherence tomography, *J. Biomed. Opt.*, 2007, **12**, 034009.

77 C. Dai, X. Liu and S. Jiao, Simultaneous optical coherence tomography and autofluorescence microscopy with a single light source, *J. Biomed. Opt.*, 2012, **17**, 080502.
78 H. Pahlevaninezhad, A. M. D. Lee, G. Hohert, S. Lam, T. Shaipanich, E.-L. Beaudoin, C. MacAulay, C. Boudoux and P. Lane, Endoscopic high-resolution autofluorescence imaging and OCT of pulmonary vascular networks, *Opt. Lett.*, 2016, **41**, 3209–3212.
79 J. Mavadia, J. Xi, Y. Chen and X. Li, An all-fiber-optic endoscopy platform for simultaneous OCT and fluorescence imaging, *Biomed. Opt. Express*, 2012, **3**, 2851–2859.
80 H. Chen, H. Wang, M. N. Slipchenko, Y. K. Jung, Y. Shi, J. Zhu, K. K. Buhman and J. X. Cheng, A multimodal platform for nonlinear optical microscopy and microspectroscopy, *Opt. Express*, 2009, **17**, 1282–1290.
81 J. Rehbinder, L. Brückner, A. Wipfler, T. Buckup and M. Motzkus, Multimodal nonlinear optical microscopy with shaped 10 fs pulses, *Opt. Express*, 2014, **22**, 28790–28797.
82 D. Li, W. Zheng, Y. Zeng and J. Y. Qu, In vivo and simultaneous multimodal imaging: Integrated multiplex coherent anti-Stokes Raman scattering and two-photon microscopy, *Appl. Phys. Lett.*, 2010, **97**, 223702.
83 W. Langbein, Israel Rocha-Mendoza and Paola Borri, Coherent anti-Stokes Raman micro-spectroscopy using spectral focusing: theory and experiment, *J. Raman Spectrosc.*, 2009, **40**, 800–808.
84 P. W. Roth, A. J. Maclean, D. Burns and A. J. Kemp, Direct diode-laser pumping of a mode-locked Ti:sapphire laser, *Opt. Lett.*, 2011, **36**, 304.
85 R. Sawada, H. Tanaka, N. Sugiyama and F. Kannari, Wavelength-multiplexed pumping with 478- and 520-nm indium gallium nitride laser diodes for Ti:sapphire laser, *Appl. Opt.*, 2017, **56**, 1654.
86 M. Andreana, T. Le, A. K. Hansen, A. J. Verhoef, O. B. Jensen, P. E. Andersen, P. Slezak, W. Drexler, A. Fernández and A. Unterhuber, Epi-detecting label-free multimodal imaging platform using a compact diode-pumped femtosecond solid-state laser, *J. Biomed. Opt.*, 2017, **22**, 1.
87 K. König, P. Andersen, T. Le and H. G. Breunig, Multiphoton imaging with a novel compact diode-pumped Ti:sapphire oscillator, *Microsc. Res. Tech.*, 2015, **78**, 1154–1158.
88 A. Unterhuber, B. Považay, A. Müller, O. B. Jensen, M. Duelk, T. Le, P. M. Petersen, C. Velez, M. Esmaeelpour, P. E. Andersen and W. Drexler, Simultaneous dual wavelength eye-tracked ultrahigh resolution retinal and choroidal optical coherence tomography, *Opt. Lett.*, 2013, **38**, 4312.
89 A. Unterhuber, B. Považay, B. Hermann, H. Sattmann, W. Drexler, V. Yakovlev, G. Tempea, C. Schubert, E. M. Anger and P. K. Ahnelt, Compact, low-cost Ti: Al2O3 laser for in vivo ultrahigh-resolution optical coherence tomography, *Opt. Lett.*, 2003, **28**, 905–907.
90 T. A. Pologruto, B. L. Sabatini and K. Svoboda, ScanImage: flexible software for operating laser scanning microscopes, *Biomed. Eng. Online*, 2003, **2**, 13.
91 R. Nejati, C. Skobowiat and A. T. Slominski, Commentary on the practical guide for the study of sebaceous glands, *Exp. Dermatol.*, 2013, **22**, 629–630.
92 Y. Jung, J. Tam, H. Ray Jalian, R. Rox Anderson and C. L. Evans, Longitudinal, 3D In Vivo Imaging of Sebaceous Glands by Coherent Anti-Stokes Raman Scattering Microscopy: Normal Function and Response to Cryotherapy, *J. Invest. Dermatol.*, 2015, **135**, 39–44.
93 M. Manfredini, M. Greco, F. Farnetani, S. Ciardo, N. De Carvalho, V. D. Mandel, M. Starace and G. Pellacani, Acne: morphologic and vascular study of lesions and surrounding skin by means of optical coherence tomography, *J. Eur. Acad. Dermatol. Venereol.*, 2017, **31**, 1541–1546.